

2 Planar Pixel Sensors for the ATLAS Upgrade: Beam 3 Tests results

J. Weingarten^{1*}, S. Altenheiner², M. Beimforde³, M. Benoit⁴, M. Bomben⁵, G. Calderini^{5,6}, C. Gallrapp⁴, M. George¹, S. Gibson⁴, S. Grinstein⁷, Z. Janoska⁸, J. Jentsch⁴, O. Jinnouchi⁹, T. Kishida⁹, A. La Rosa¹⁰, V. Libov¹¹, A. Macchiolo³, G. Marchiori⁵, D. Muenstermann⁴, R. Nagai⁹, G. Piacquadio⁴, B. Ristic², I. Rubinskiy¹¹, A. Rummler², Y. Takubo¹², G. Troska², S. Tsiskaridze⁷, I. Tsurin¹³, Y. Unno¹², P. Weigell³, T. Wittig²

¹*II. Physikalisches Institut, Georg-August-Universität Göttingen, Germany*

Email: jens.weingarten@uni-goettingen.de

²*Technische Universität Dortmund, Fakultät Physik, Dortmund, Germany*

³*Max-Planck-Institut für Physik, München, Germany*

⁴*CERN, Genève, Switzerland*

⁵*Laboratoire de Physique Nucleaire et de Hautes Énergies (LPNHE), Paris, France*

⁶*Dipartimento di Fisica E. Fermi, Università di Pisa, and INFN Sez. di Pisa, Pisa, Italy*

⁷*ICREA and Institut de Fisica d'Altes Energies (IFAE), Bellaterra (Barcelona), Spain*

⁸*Division of elementary particle physics - Institute of Physics of the Academy of Sciences of the Czech Republic, Prague, Czech Republic*

⁹*Tokyo Institute Of Technology, Tokyo, Japan*

¹⁰*Section de Physique (DPNC), Université de Genève, Genève, Switzerland*

¹¹*Deutsches Elektronen-Synchrotron (DESY), Hamburg, Germany*

¹²*High Energy Accelerator Research Organization, Tsukuba, Japan*

¹³*The University of Liverpool, Liverpool, United Kingdom*

4

ABSTRACT: The performance of planar silicon pixel sensors, in development for the ATLAS Insertable B-Layer and High Luminosity LHC (HL-LHC) upgrades, has been examined in a series of beam tests at the CERN SPS facilities since 2009. Salient results are reported on the key parameters, including the spatial resolution, the charge collection and the charge sharing between adjacent cells, for different bulk materials and sensor geometries.

5 Measurements are presented for n⁺-in-n pixel sensors irradiated with a range of fluences and for p-type silicon sensors with various layouts from different vendors. All tested sensors were connected via bump-bonding to the ATLAS Pixel read-out chip.

The tests reveal that both n-type and p-type planar sensors are able to collect significant charge even after the lifetime fluence expected at the HL-LHC.

6 KEYWORDS: Silicon pixel detectors, planar sensors, radiation damage to detector materials (solid
7 state), beam tests, simulations, ATLAS upgrade, HL-LHC, SLHC.

9 Contents

10	1. Introduction	1
11	2. Beam test setup	2
12	2.1 The EUDET telescope	3
13	2.2 Devices Under Test	3
14	3. The beam test analysis	4
15	3.1 Track reconstruction	4
16	3.2 Detector alignment	4
17	3.3 Data analysis	5
18	4. The n-in-p demonstrator program	6
19	4.1 CiS sensors	6
20	4.1.1 Sensor design	7
21	4.1.2 Beam test results	8
22	4.2 HPK sensors	11
23	4.2.1 Sensors design	12
24	4.2.2 Beam test results	14
25	5. Radiation hardness of n-in-n sensors	15
26	5.1 Results	17
27	6. Slim Edge	20
28	7. Conclusion	22

30 1. Introduction

31 The ATLAS collaboration will upgrade the current Pixel Detector [1] in two phases. A first upgrade
 32 will be realized during the shut-down in 2013, by inserting a fourth detection layer (Insertable B-
 33 Layer - IBL) at a radius of 3.2 cm from the beam line. The IBL will improve the tracking and
 34 vertexing performance of the current pixel detector significantly during operation of the LHC at its
 35 nominal centre-of-mass energy ($\sqrt{s} = 14$ TeV) [2].

36 The close proximity to the interaction point imposes a very harsh radiation environment on the
 37 IBL. At the end of Phase-I operation of the LHC, foreseen around 2020, the IBL must sustain an
 38 estimated fluence of 5×10^{15} n_{eq}/cm², including a 60% safety factor at $r = 3.2$ cm.

*Corresponding author.

39 The Phase-II luminosity upgrade for the LHC (beyond 2020) aims to increase the instanta-
40 neous luminosity to $5 \times 10^{34} \text{ cm}^{-2} \text{ s}^{-1}$, posing a serious challenge to the technology for the AT-
41 LAS tracker in the High Luminosity era (HL-LHC): the lifetime fluence for the innermost layer,
42 including safety factors, is estimated to be on the order of $2 \times 10^{16} \text{ n}_{\text{eq}}/\text{cm}^2$ [3]. Hence, in view of
43 a possible pixel system replacement after 2020, new pixel sensors are under study.

44 Within the Planar Pixel Sensor collaboration (PPS) [7] several optimizations of this well-
45 known technology are under investigation, to address issues arising from the LHC upgrades. The
46 PPS collaboration investigates the suitability of different materials (p- and n-bulk, diffusion oxy-
47 genated float zone, magnetic Czochralski), different geometries (slim edge design, number and
48 width of guard rings) and different biasing / isolation choices (punch-through, polysilicon resis-
49 tance / p-spray, p-stop), for a new generation of planar pixel sensors. Data taken during beam
50 tests complement tests under laboratory conditions in assessing the performance of various sensor
51 prototypes. In this paper results from two beam test campaigns in 2010 are presented.

52 The paper is organized as follows. After a description of the experimental setup of the beam
53 tests in Section 2 and some details of the data analysis in Section 3, beam test results are presented
54 on three areas of the scientific program of the PPS collaboration:

55 Sensors implemented in p-type silicon are being studied by several groups within the PPS
56 collaboration. Section 4 shows results from the first beam test operation of various prototype
57 sensors. We will show that the performance of p-type sensors in terms of collected charge ¹, charge
58 sharing probability, and spatial resolution is very similar to that of n-type sensors.

59 In Section 5 the radiation-hardness of sensors implemented in n-type diffusion oxygenated
60 float-zone silicon are studied. We will show that n-in-n detectors are operable at the nominal bias
61 voltage of 1000 V after a fluence comparable with that expected for IBL ($5 \times 10^{15} \text{ n}_{\text{eq}}/\text{cm}^2$). Noise
62 occupancy, charge collection performance, charge sharing probability and spatial resolution will be
63 presented.

64 The new pixel sensors will not only have to sustain the harsher environment, but also have to
65 show high geometrical acceptance without overlapping adjacent modules. Hence the inactive areas
66 of the future pixel sensor have to be reduced significantly. For this reason, efforts were devoted
67 to design detectors with reduced dead area. The “slim edge” detector-concept will be presented in
68 Section 6, together with its performance in terms of charge collection at the detectors’ edge.

69 **2. Beam test setup**

70 Beam tests are crucial for characterizing the performance of any particle detector. Planar silicon
71 sensors for the ATLAS upgrade have been evaluated in several beam tests in 2009 and 2010. Data
72 presented in this paper were taken in two different periods in 2010 at the CERN SPS beamline H6.
73 In both periods pion beams of 120 GeV/c were used. The high momentum of the beam particles
74 minimizes the influence of multiple scattering, enabling high precision tracking using the EUDET
75 beam telescope [8].

¹collected charge is always presented as Most Probable Value (MPV), if not stated otherwise

76 **2.1 The EUDET telescope**

77 The telescope consists of six equal planes, divided into two groups (arms) of three planes each.
78 The Devices Under Test (DUTs) are mounted in between these two arms of the telescope as well as
79 downstream of the last telescope plane. The increase of the track extrapolation error downstream
80 of the telescope was minimized by mounting the DUTs as close as possible to the last telescope
81 plane.

82 The sensitive elements of the telescope planes are Mimosas26 [25] active pixel sensors with a
83 pixel pitch of $18.4\ \mu\text{m}$. Each plane consists of 1152×576 pixels covering an active area of
84 $21.2 \times 10.6\ \text{mm}^2$. The tracking resolution between the telescope arms is estimated to be $2\ \mu\text{m}$,
85 at the position of the samples downstream of the telescope it is approximately $10\ \mu\text{m}$. [26]

86 A coincidence of four scintillators (two upstream and two downstream of the telescope) was used
87 for triggering, which resulted in an effective sensitive area of $2 \times 1\ \text{cm}^2$.

88 **2.2 Devices Under Test**

89 All DUTs were read out using the current ATLAS Pixel readout chip (FE-I3) [9]. The FE-I3 chip
90 is an array of 160 rows \times 18 columns of $50\ \mu\text{m} \times 400\ \mu\text{m}$ read-out cells. In each readout cell the
91 sensor charge signal is amplified and compared to a programmable threshold by a discriminator.
92 The information on the collected signal is encoded through a digital time over threshold (ToT) [9]
93 measured in units of 25 ns, which is the nominal LHC bunch crossing rate. The ToT to charge
94 conversion was tuned for each individual pixel to 60 ToT for a deposited charge of 20 ke. Discrim-
95 inator thresholds were tuned to a charge of 3.2 ke. Prior to the beam test, tuning was performed
96 for every readout chip in realistic conditions, designed to closely resemble those at the beam test.
97 Since the ToT-tuning is particularly temperature dependent, the ToT was calibrated on each sample
98 after installation in the beam test setup to ensure a proper charge conversion.

99 For each DUT a fiducial region was defined, based on geometrical and operability consider-
100 ations. For most studies only the performance of central pixels is of interest. Therefore in many
101 analyses the pixels at the edges of the sensors were masked. In addition, all pixels that were found
102 to have disconnected or merged bump-bonds in laboratory measurements were masked, as were
103 pixels with high noise occupancy.

104 Devices were irradiated to different fluences using 25 MeV energy protons at the Irradiation
105 Center in Karlsruhe [19], 24 GeV/c momentum protons at the CERN PS irradiation facility [12]²,
106 and reactor neutrons at the TRIGA reactor of the Jožef Stefan Institute, Ljubljana [18]. The radi-
107 ation damage from the different irradiations is scaled to the equivalent damage from 1 MeV neu-
108 trons using the NIEL hypothesis [30]. During the irradiations the devices were neither powered
109 nor cooled. No standardized annealing procedure was used, but samples were stored below $0\ \text{°C}$
110 to avoid uncontrolled annealing. The FE-I3 was designed for a lifetime irradiation dose of 1 kGy.
111 Some of the DUTs were irradiated to significantly higher doses, leading to increasing numbers of
112 non-working pixels.

113 For the beam tests, irradiated DUTs were cooled via a strip of copper tape thermally connecting
114 the backside of the DUTs with the base plate of the thermal enclosure. The base plate was in turn
115 cooled using dry ice (CO_2) [17]. Due to this setup, the temperature of the sensors varied over time

²we observed FE-I3 chip stopped working after being CERN PS irradiated

116 as the dry ice evaporated and needed to be closely monitored. Temperatures were recorded, ranging
117 between $-45\text{ }^{\circ}\text{C}$ shortly after filling the coldbox with dry ice and $-15\text{ }^{\circ}\text{C}$ towards the end of a data
118 taking period.

119 **3. The beam test analysis**

120 **3.1 Track reconstruction**

121 The tracks of particles traversing the EUDET telescope are reconstructed from raw hit positions
122 by a sequential algorithm. In the first step, the hits recorded in all telescope planes and DUTs
123 are converted into the EU Telescope [23] internal data format. A time stamp issued by the Trigger
124 Logic Unit (TLU) [24] is attached to each hit, enabling recovery from any loss of synchronisation
125 between telescope and DUTs during this step, provided the desynchronisation is not too severe.

126 As the Mimosas26 sensors of the telescope plane use the rolling shutter read-out technique, the
127 telescope integrates hits for $112\text{ }\mu\text{s}$ after the arrival of the trigger signal. This is much longer than
128 the 400 ns hit-buffer of the DUTs, so some tracks will be recorded by the telescope, but not by the
129 DUTs. To correct for this effect, only hits that were recorded within the sensitive time of the DUTs
130 are retained for further analysis. This is done by requesting hits spatially associated to the track in
131 one or more of the other DUTs (in-time tracks). A clustering algorithm is then executed searching
132 for clusters in all planes.

133 Hits are then transformed from the local coordinate system of each plane to a global coordinate
134 system, where the z-axis gives the beam direction. During this coordinate transformation the pixel
135 sizes in x- and y-directions, the specified z-position of all sensors, and the rotations of the DUTs
136 about all axes are taken into account. Based on correlations between hit positions in different planes
137 in the global frame, a coarse pre-alignment is calculated. Using this information, the alignment
138 processor (see also 3.2) tries to fit tracks through all planes in the setup, taking into account the
139 different spatial resolutions of the planes and individual track selection criteria for each plane.
140 Individual selection criteria are especially necessary, since the pixel size of the telescope-planes
141 is $18.4\text{ }\mu\text{m}$ in both directions, whereas the investigated FE-I3 based samples have a pixel size of
142 $400\text{ }\mu\text{m} \times 50\text{ }\mu\text{m}$.

143 The final step is the track-fitting, which is based on a Kalman filter [29]. The track fits are
144 unbiased, requiring a hit in at least four out of the six telescope planes and in at least one DUT. Also
145 in this step, different track selection criteria can be applied. The parameters of all reconstructed
146 tracks are finally stored in a ROOT file [31] for further analysis (see Section 3.3).

147 **3.2 Detector alignment**

148 The alignment for the telescope planes and the DUTs in the EU Telescope track-reconstruction uses
149 the MILLIPEDE tool [27]. In the algorithm the alignment constants are calculated such that the
150 uncertainties of the fitted track parameters, as well as the χ^2 of the track residuals, are minimized.
151 Straight line fits to the hit positions in all active planes are performed independently for the x- and y-
152 directions. Individual criteria can be applied to the resulting residual distributions to suppress fake
153 tracks. In the alignment process the pre-alignment constants, calculated in the previous hitmaker
154 step, are taken into account. This enables alignment of all telescope-planes and DUTs in one step,

155 where just the first telescope-plane is fixed in its position and orientation. The alignment constants
156 are applied in the final track fitting process.

157 **3.3 Data analysis**

158 The analysis of the reconstructed tracks is conducted in several steps, using a dedicated data anal-
159 ysis framework (tbmon) [28].

160 Firstly, unresponsive and noisy pixels are identified and masked. A pixel is unresponsive if
161 it registers no hit during the full data taking period and noisy if more than 5×10^{-4} of all hits
162 registered in this pixel are not correlated with a beam particle. Typically, less than 1 % of pixels are
163 masked in non-irradiated modules; for irradiated devices the fraction fluctuates between samples.
164 On average, roughly 10 % of the pixels have to be masked due to problems with settings of the
165 readout chip or increased noise due to high leakage current of the sensor.

166 In the following analyses tracks extrapolated from the telescope are “matched” to a hit if the hit
167 and the extrapolated track impact point in the DUT plane containing the hit are closer than $400 \mu\text{m}$
168 in the long pixel direction and $150 \mu\text{m}$ in the short pixel direction. The hit position is defined as
169 the η corrected ToT weighted position of all pixels in a cluster [13].

170 To estimate the intrinsic spatial resolution of the DUTs the distribution of hit residuals is
171 studied. The hit residual is defined as the distance between the reconstructed hit position on the
172 DUT and the extrapolation of the fitted track to the DUT plane. The intrinsic spatial resolution
173 is estimated by the RMS of the residual distribution for clusters of all sizes, while the residual
174 distribution of 2-pixel clusters is used to estimate the width of the area between pixels, where
175 charge sharing occurs. The distribution is fitted with the sum of two Gaussian functions, where one
176 accounts for mis-reconstructed hits, resulting in large residual values (equal to 2 times the pixel
177 pitch or more), and the other for correctly reconstructed hits. The width of this “core” Gaussian
178 gives the width of the charge sharing region.

179 To calculate the charge sharing probability for each hit within a cluster, it is determined
180 whether a hit is found in a pixel cell adjacent to the one matched to a track. This probability
181 increases towards the edge of the pixel since charge carriers are more likely to drift to the neigh-
182 bouring pixel. The corresponding plot, referred to as a charge sharing map, is centred on one pixel,
183 also showing half of the adjacent pixel in each direction. The overall charge sharing is defined
184 as the number of tracks with at least one hit in a neighbouring pixel divided by the number of all
185 tracks.

186 Due to a problem in the readout system, random DUTs stopped sending data for random short
187 intervals. Therefore, the availability of a reference plane for the selection of in-time tracks cannot
188 be ensured at all times. As this selection is crucial for the measurement of the hit efficiency, this
189 analysis could not be done with the available data, while charge collection and spatial resolution
190 measurements are unaffected.

191 Most of the hits registered by the DUTs were anyway associated with tracks; this can be seen
192 from the LVL1 distribution. The LVL1 distribution (see Figure 1) shows the arrival time of every
193 recorded hit with respect to the external trigger signal. The very pronounced peak shows that
194 most hits have a strong correlation with the timing of the external trigger signal, meaning that they
195 are indeed generated by the triggered particle traversing the DUT. By applying cuts to the LVL1
196 distribution, we can therefore suppress most hits that are not associated to a track.

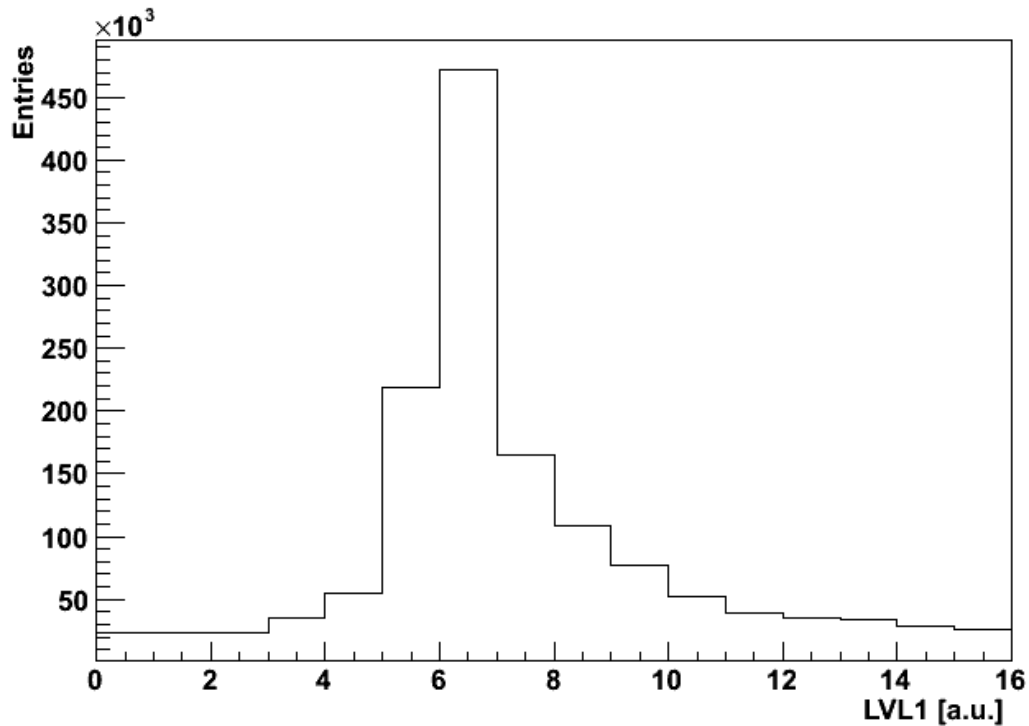


Figure 1. Example of LVL1 distribution.

197 **4. The n-in-p demonstrator program**

198 While n-type bulk sensors require patterned guard rings on the back side of the sensor, for p-type
 199 material these can be moved to the pixelated side of the sensor (front side); then metallization is
 200 the only process for the back side. This makes it a very cost-effective material for future pixel
 201 detectors. On the other hand the high voltage, which is applied to the back side of the sensor, is
 202 also present on the edges of the front side of the sensor facing the read-out chip, which is at ground
 203 potential. Thus spark discharges may occur, posing a risk to the readout electronics itself. This can
 204 be limited by the deposition of an insulating coating on the edge of the sensor; more details are
 205 given in the next section.

206 Sensors in p-type technology tested in 2010 were produced at CiS³ and at HPK⁴. Table 1 summa-
 207 rizes the relevant quantities for the devices studied in the beam test. Further details of each sample
 208 are described below.

209 **4.1 CiS sensors**

210 In the following the p-type sensors produced at CiS will be introduced and their beam test results
 211 discussed.

³Forschungsinstitut für Mikrosensorik und Photovoltaik GmbH

⁴Hamamatsu Photonics K. K.

sample	Period	fluence ($10^{15} n_{eq}/cm^2$)	irradiation type	V_{bias} [V]
MPP1	July	0	–	150, 200
MPP2	July	0	–	150, 200
MPP3	October	0	–	150
MPP4	October	1	reactor neutrons	250, 350, 500, 550, 700
MPP5	October	1	25 MeV protons	500, 550
KEK1	October	0	–	100, 200
KEK2	October	0	–	100, 200

Table 1. Relevant quantities of the n-in-p samples.

212 4.1.1 Sensor design

213 The n-in-p pixel sensors labelled as MPP1–MPP5 were produced at CiS with a geometry compat-
 214 ible with FE-I3, in the framework of a common RD50 production [20]. They were made from
 215 Diffusion Oxygenated Float Zone (DOFZ) 285 μm thick wafer, with $\langle 100 \rangle$ crystal orientation
 216 and a wafer resistivity of 15 $\text{k}\Omega\text{cm}$. The depletion voltage before irradiation was nominally 60 V.

217 Two guard rings structures with differing widths have been implemented and tested. One
 218 design has the standard inactive area of 1 mm per side of normal ATLAS pixel sensors, while the
 219 other has a reduced inactive area, as illustrated in Figure 2. MPP1, MPP3 and MPP5 have 19
 220 guard-rings, with the standard total inactive width of 1 mm on each side. The samples MPP2 and
 221 MPP4 (see Table 1) have 15 guard-rings with a total inactive area of 610 μm on each side. For both
 222 guard rings designs the bias ring and the inner guard ring are wider than the other ones, enabling
 223 tests of the sensors before connection to the read-out chips. The external guard ring widths grows
 224 with promixity to the cutting edge from 17 μm to 22 μm , with the gap between the rings from 5
 225 to 8 μm . The distance between the last ring and the dicing edge is 400 μm for the 19 guard rings
 226 design while it is 100 μm in the 15 guard rings design.

227 The inter-pixel isolation is achieved by means of a homogenous p-spray implantation.

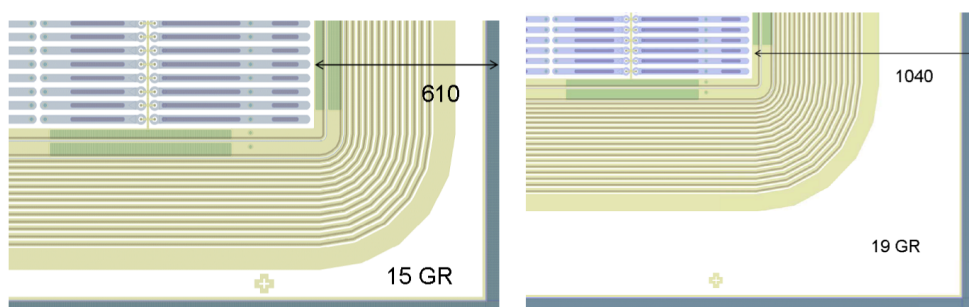


Figure 2. Left: View of a corner of an n-in-p sensor of the CiS production with 15 guard rings. Right: View of a corner of an n-in-p sensor of the CiS production, with 19 guard rings.

228 A BCB (Benzocyclobutene) coating has been applied to the pixelated side of the n-in-p pixel
 229 sensors, to prevent sparks between the area outside the guard ring area, that is at the same high

230 potential as the back side, and the chip, at ground potential (Figure 3). The interconnection to the
 231 chips has been performed via bump-bonding at IZM-Berlin ⁵.

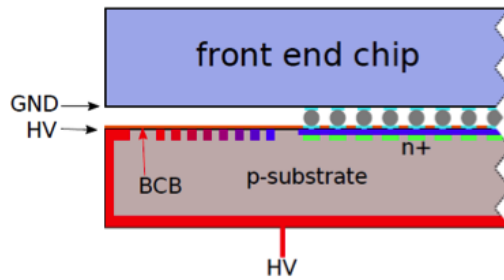


Figure 3. Schematics of a CiS n-in-p pixel assembly. The potential of the different parts is given. The BCB layer is indicated in orange.

232 4.1.2 Beam test results

233 As documented in Table 1, during the first beam test period (July 2010) none of the CiS n-in-
 234 p sensors (namely MPP1, MPP2) were irradiated. In the second period (October 2010) MPP4
 235 was tested after irradiation with reactor neutrons [18] to a fluence of $1 \times 10^{15} \text{ n}_{\text{eq}}/\text{cm}^2$ and MPP5
 236 was irradiated with low energy protons (25 MeV) at the cyclotron of the Karlsruhe Institute of
 237 Technology (KIT) [19] to the same equivalent fluence. MPP3 was kept as an unirradiated reference.
 238 The performance of these five samples is presented as follows.

239 **Cluster size** The cluster size distribution was studied for all sensors as a function of the bias
 240 voltage. A detailed breakdown is reported in Table 2. For the non-irradiated sample roughly 70 %
 241 of the clusters consisted of a single hit. A further 25 % were two-hit clusters, while the remainder
 242 were three or more hit clusters.

243 Due to trapping effects and lower overall charges for irradiated sensors, one hit clusters are
 244 more often observed than in unirradiated samples. With increasing bias voltage the number of two
 245 hit clusters rises since it becomes more likely that a neighbouring pixel is above threshold as well.
 246 This behaviour can be clearly seen in Figure 4.

247 **Collected charge** The collected charge was measured as a function of the bias voltage for the
 248 different sensors. In Figure 5 the sub-pixel resolved charge collection profile is shown for MPP3
 249 at V_{bias} of 150 V. The most prominent feature is the lower collected charge value on the right hand
 250 side, corresponding to the bias dot region where the pixel implant is connected to the bias grid.
 251 The same effect is evident in n-in-n devices with the same design (Section 5). In this region the
 252 collected charge is still well above the threshold.

253 Figure 6 shows lower collected charge along the edges of a pixel, due to charge sharing with the
 254 neighboring pixels. As charge sharing occurs, less charge is available for the pixel traversed by
 255 the particle, decreasing the probability to pass the electronics threshold. This effect is especially

⁵Fraunhofer-Institut für Zuverlässigkeit und Microintegration, Berlin

sample	V_{bias} [V]	CS=1 [%]	CS=2 [%]	CS=3 [%]	Charge sharing probability [%]
MPP1	150	65	31	2	33
MPP1	200	60	36	2	37
MPP2	200	75	23	1	24
MPP3	150	71	25	1	27
MPP4	250	95	4	1	4
MPP4	350	92	6	1	7
MPP4	500	88	9	1	10
MPP4	550	87	11	1	11
MPP4	700	85	13	1	14
MPP5	500	87	11	1	12
MPP5	550	78	19	1	21

Table 2. Cluster size (CS) composition for CiS modules measured at different bias voltages during beam tests; clusters were matched to a track. Charge sharing probability is also reported.

- MPP4, $\theta = 0^\circ$, CS = 1 ▲ MPP4, $\theta = 0^\circ$, CS = 2 ▼ MPP4, $\theta = 0^\circ$, CS = 3
- MPP5, $\theta = 0^\circ$, CS = 1 ▲ MPP5, $\theta = 0^\circ$, CS = 2 ▼ MPP5, $\theta = 0^\circ$, CS = 3
- MPP3, $\theta = 0^\circ$, CS = 1 ▲ MPP3, $\theta = 0^\circ$, CS = 2 ▼ MPP3, $\theta = 0^\circ$, CS = 3

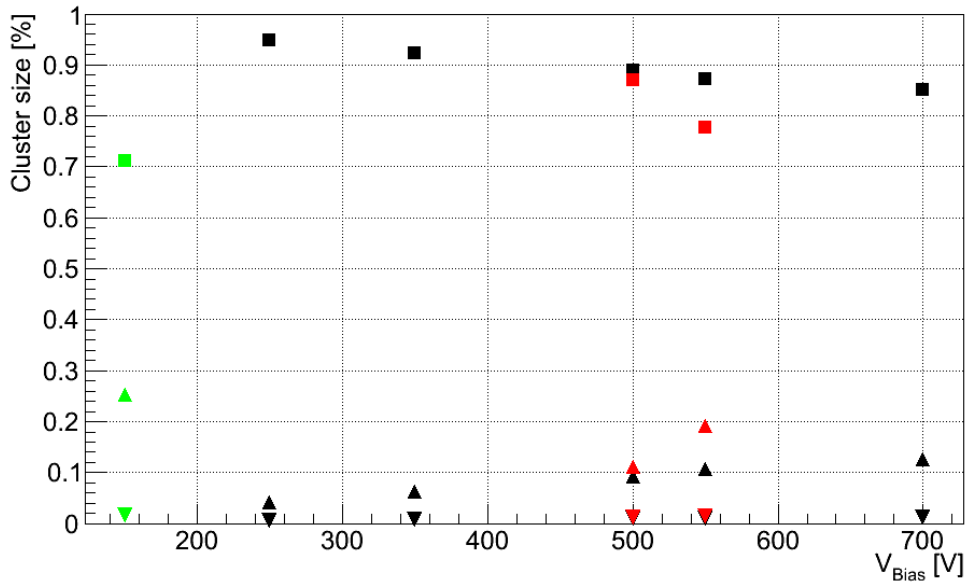


Figure 4. Relative cluster size abundance as a function of bias voltage for irradiated MPP4 and MPP5 devices. MPP3 (non-irradiated) are added for comparison. Particles were impinging at normal incidence. Errors on fractions are negligible and so not visible in the plot.

256 pronounced in the corners of the pixel, as charge can be shared among four pixels. However, in
 these regions the deposited charge is still high enough for an efficient operation of the device.

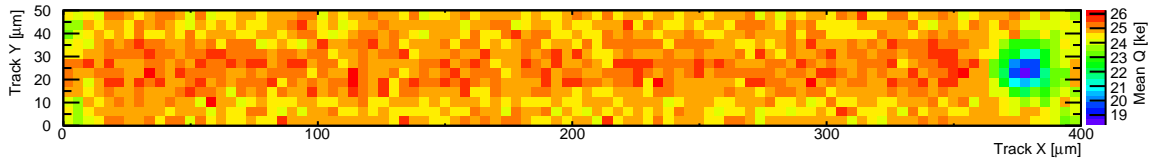


Figure 5. Charge collection within a single pixel by track position for MPP3 at V_{bias} of 150 V

257

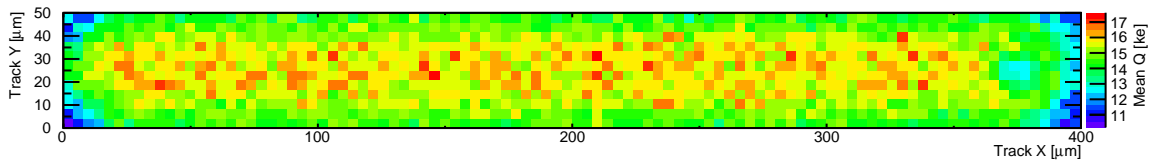


Figure 6. Charge collection within a single pixel by track position for MPP5 at $V_{\text{bias}} = 500$ V

258 Figure 7 shows the most probable charge for all samples. For comparison the charge collected
 259 by unirradiated devices (MPP1 and MPP2) is included and a typical discriminator threshold of
 260 3200 e is indicated. A systematic error on the collected charge of 400 e is assumed, due to the finite
 261 charge resolution of the ToT mechanism; a 5% systematic uncertainty is taken into account, due to
 262 non-uniformity in the injection capacitances.

263 Although the irradiated samples do not show saturation of the collected charge up to 700 V,
 264 already at low bias voltages the collected charge exceeds the electronics threshold by more than a
 265 factor of two and can thus be considered safe for tracking applications.

266 **Charge sharing** In Figure 8 (top) the charge sharing probability within one pixel for MPP3 is
 267 shown. At normal track incidence increased charge collection probability is evident at the edges
 268 and corners of the pixel. The situation after irradiation is shown in Figure 8 (bottom). Here the
 269 charge sharing especially on the side of the punch through biasing is reduced, since there is a higher
 270 probability for the neighbouring pixel to be below threshold. This is also reflected in the average
 271 charge sharing probability given in Table 2 for the n-in-p CiS detectors in all states. With increasing
 272 bias voltage an increase of the charge sharing is observed for the irradiated sensors (MPP4, MPP5)
 273 due to the increase in the collected charge.

274 **Residuals** Figure 9 shows the cluster position residual distribution for the irradiated module
 275 MPP5, biased at 500 V. The spatial resolution is compatible with the digital resolution, as one-
 276 hit clusters are dominant. For comparison, the residual distribution for MPP3 at 150 V is shown in
 277 Figure 10. No difference is appreciable between the two samples.

278 For the irradiated assembly MPP5 Figure 11 shows in case of two hit clusters a resolution of
 279 $(7.2 \pm 2.5) \mu\text{m}$ in the core gaussian along the short pixel direction. For comparison, Figure 12 shows
 280 the two-hit cluster residuals for MPP3 at 150 V. After irradiation there are more noise related hits,

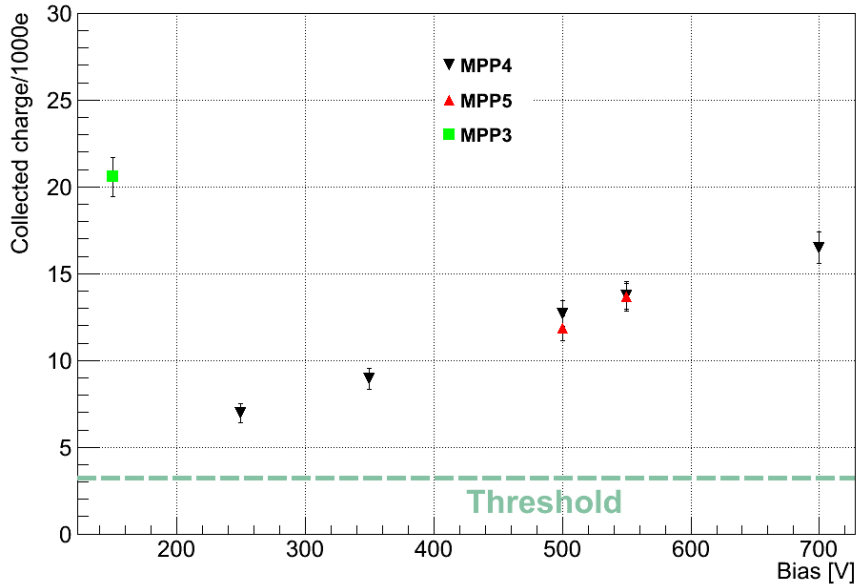


Figure 7. Charge collected in a cluster: most probable value of the charge distribution fitted to a Landau function convoluted with a gaussian as a function of the bias voltage. See text for the discussion on the assigned systematic uncertainty. The threshold value is also depicted as a dashed line.

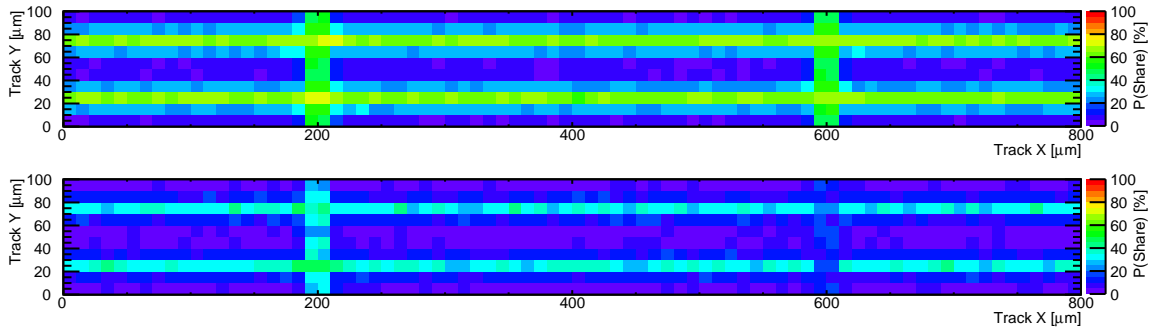


Figure 8. Charge sharing map for MPP3 detector, biased at 150 V (top) and for MPP4 detector, biased at 700 V.

281 clearly visible in Figure 11. The fitted core fraction indeed decreases with respect to unirradiated
 282 sample (Figure 12). Nonetheless, the tracking capabilities of irradiated DUTs, in terms of spatial
 283 resolution, are still satisfactory.

284 4.2 HPK sensors

285 In the following the p-type sensors produced at HPK will be introduced and their beam test results
 286 discussed.

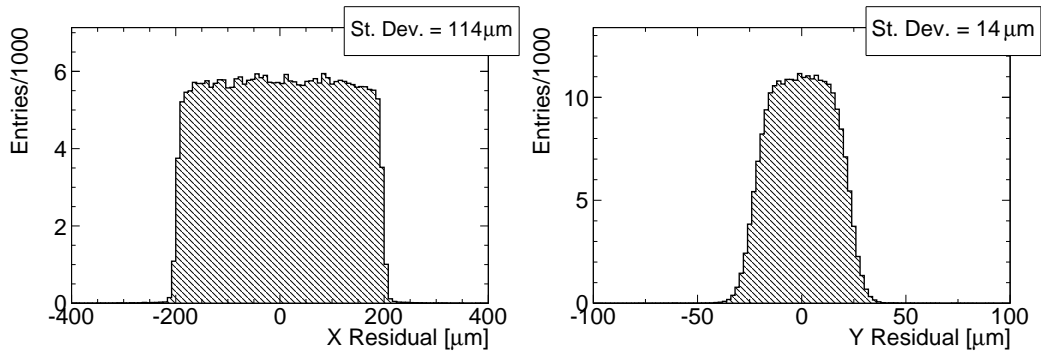


Figure 9. Residual distribution for irradiated sample MPP5 at V_{bias} of 500 V. Left: long pixel projection; right: short pixel projection.

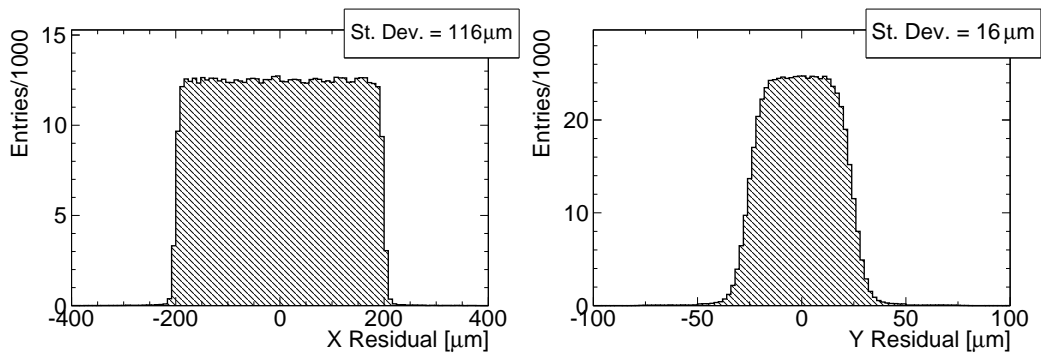


Figure 10. Residual distribution for non-irradiated MPP3 biased at 150 Volts. Left: long pixel projection; right: short pixel projection.

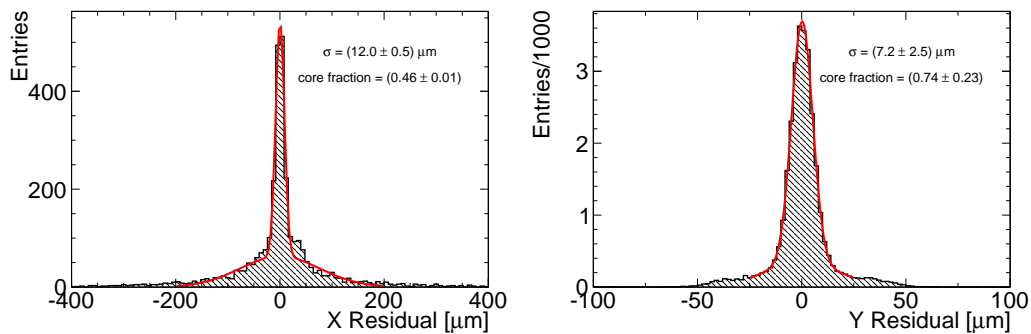


Figure 11. Residual distribution for irradiated sample MPP5 biased at V_{bias} of 500 V, for two-hit clusters. Left: long pixel projection; right: short pixel projection.

287 **4.2.1 Sensors design**

288 Two modules with different sensor n-in-p layouts were subject to beam tests; one with a polysilicon
 289 bias resistor and a common p-stop isolation (KEK1), and the other with a polysilicon bias resistor

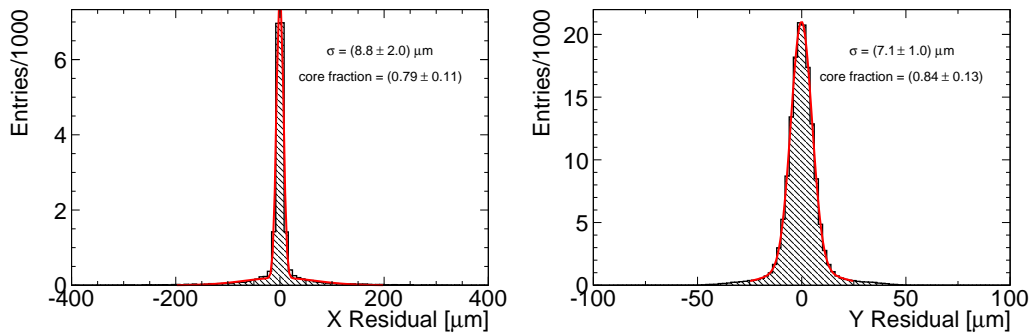


Figure 12. Residual distribution for unirradiated sample MPP3 at V_{bias} of 150 V, for two-hit clusters. Analysis restricted to clusters with 2 pixels. Left: long pixel projection; right: short pixel projection.

290 and an individual p-stop isolation (KEK2). Figure 13 shows a sketch of the pixel cell design for
 291 these two samples. The sensors came from Float Zone (FZ) wafers with $\langle 100 \rangle$ crystal orientation; the wafer thickness was 320 μm . The measured wafer resistivity was approximately 6 $\text{k}\Omega\text{cm}$.

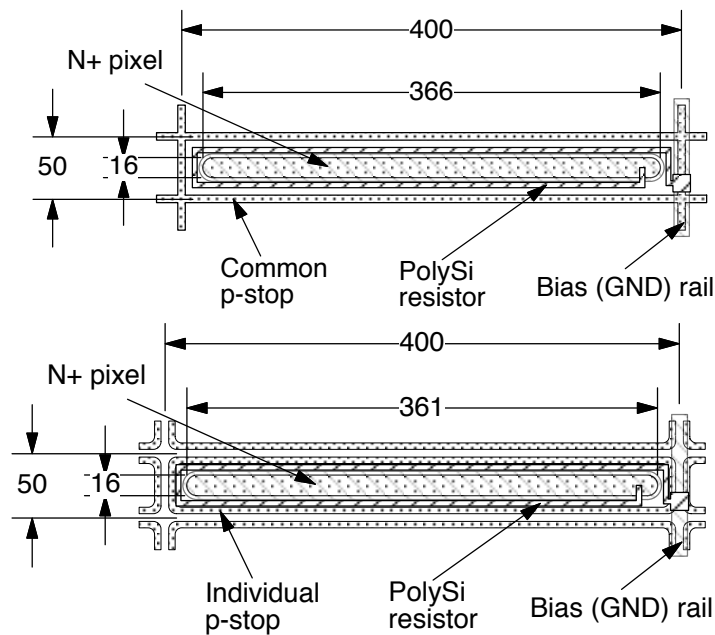


Figure 13. Pixel cell design details for KEK1 (top) and KEK2 (bottom) samples.

292

293 A metal bias rail runs along each pixel double-column; there is no bias rail implant underneath
 294 it [22]. A parylene coating has been applied to the whole body of the pixel modules, after mounted
 295 on and connected to the single-chip test card (SCC) with wire-bonding.

296

297 These modules were beam-tested before any irradiation in 2010, irradiated afterward and
 298 tested in the beamtests in 2011. The results before irradiation are reported in this paper; those
 after irradiation are being analyzed and they will be presented in a different communication. The

299 depletion voltage before irradiation was about 180 V.

300 4.2.2 Beam test results

301 The HPK samples characterization has been carried out by measuring the cluster size, collected
302 charge, charge sharing and spatial resolution as a function of the bias voltage.

303 **Cluster Size** The KEK1 and KEK2 samples were biased at 100 V and 200 V. The two samples
304 perform in a similar way in terms of cluster size for particles at normal track incidence. As shown
305 in Table 3 (see also Figure 14) more than 80% of the clusters have just one hit pixel at 100 V bias
306 voltage. As the bias voltage increases, the fraction of 2-pixel clusters also increases, as more charge
307 is collected. Therefore the charge fluctuations are small compared to the threshold, which reduces
308 the probability of a pixel collecting a signal below threshold.

sample	V_{bias} [V]	CS=1 [%]	CS=2 [%]	CS=3 [%]	Charge sharing probability [%]
KEK1	100	81	16	1	18
KEK1	200	73	23	2	26
KEK2	100	83	14	1	16
KEK2	200	76	20	2	22

Table 3. Cluster composition for HPK detectors for different bias voltages; charge sharing probability is reported in the last column. Clusters were matched to a track.

309 **Collected charge** In Figure 15 the collected charge per cluster is shown as a function of bias
310 voltage for the KEK sensors. The charge collection improves with bias voltage, but already at
311 100 V the signal is more than 4 times the threshold. At 200 V the expected full charge is collected.

312 **Charge sharing** Figure 16 shows the charge sharing map for KEK1. At normal incidence the
313 fraction of charge sharing is more than 25 % for a sensor biased at 200 V. Results for KEK2 show
314 that the charge sharing is less effective (22 %): this can be related to the different layout between
315 the two sensors. In the bottom figure the combined effect of the bias metal rail and the individual
316 p-stop is visible. Results are summarized in Table 3.

317 **Residuals** Figure 17 shows the residual distribution for all clusters at normal track incidence.
318 The spatial resolution is about $16 \mu\text{m}$ along the short pixel direction, which is comparable with the
319 digital resolution of $\text{pitch}/\sqrt{12}$; the same is true for the long pixel direction (RMS about $116 \mu\text{m}$).
320 No difference is noticeable between KEK1 and KEK2 sensors.

321 Figure 18 shows the residual distribution for two-hit clusters. For these, the spatial resolution
322 is found to be around $7 \mu\text{m}$ in the short pixel direction and around $9 \mu\text{m}$ for the long one (see
323 also Table 4). The spatial resolution when the cluster contains two hits is larger than the telescope
324 pointing-resolution and gives an estimate of the charge sharing region between neighbouring pixels.

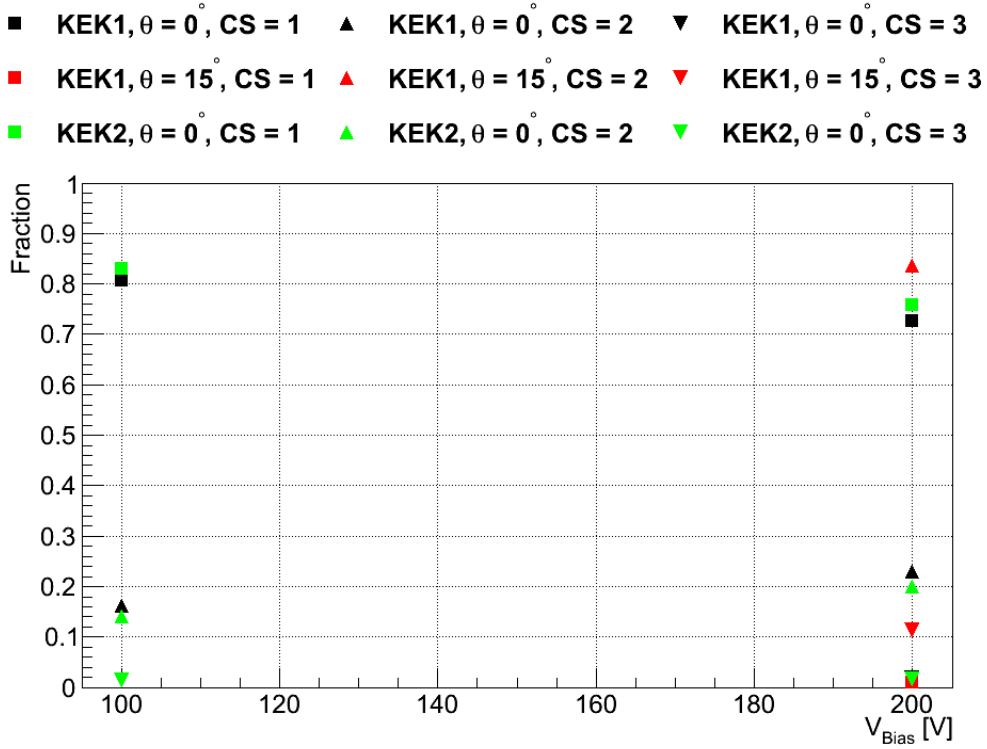


Figure 14. Fraction of cluster sizes as function of the bias voltage for HPK samples; particles were impinging at different angles too.

Sample	V_{bias} [V]	pitch (μm)	RMS (μm)	core σ (μm)	core fraction [%]
KEK1	100	400	116.00 ± 0.14	9.00 ± 0.13	68
KEK2	100	400	115.00 ± 0.14	9.40 ± 0.20	53
KEK1	200	400	116.10 ± 0.20	9.0 ± 3	74
KEK2	200	400	115.00 ± 0.15	9.31 ± 0.18	60
KEK1	100	50	16.000 ± 0.020	7.14 ± 0.06	78
KEK2	100	50	15.800 ± 0.020	6.88 ± 0.05	78
KEK1	200	50	15.90 ± 0.05	7.1 ± 1.6	80
KEK2	200	50	16.000 ± 0.021	6.81 ± 0.05	79

Table 4. Summary of residual results for KEK1 and KEK2 samples. Core σ and fraction are evaluated for 2-pixels clusters only.

325 5. Radiation hardness of n-in-n sensors

326 The n-in-n sensor technology used in the current ATLAS Pixel detector have been tested to fluences
 327 up to $1.1 \times 10^{15} \text{ n}_{eq}/\text{cm}^2$ [11]. To evaluate the usability of n-type bulk material for IBL and future
 328 detector upgrades, sensors have been irradiated with fluences as high as $2 \times 10^{16} \text{ n}_{eq}/\text{cm}^2$ using

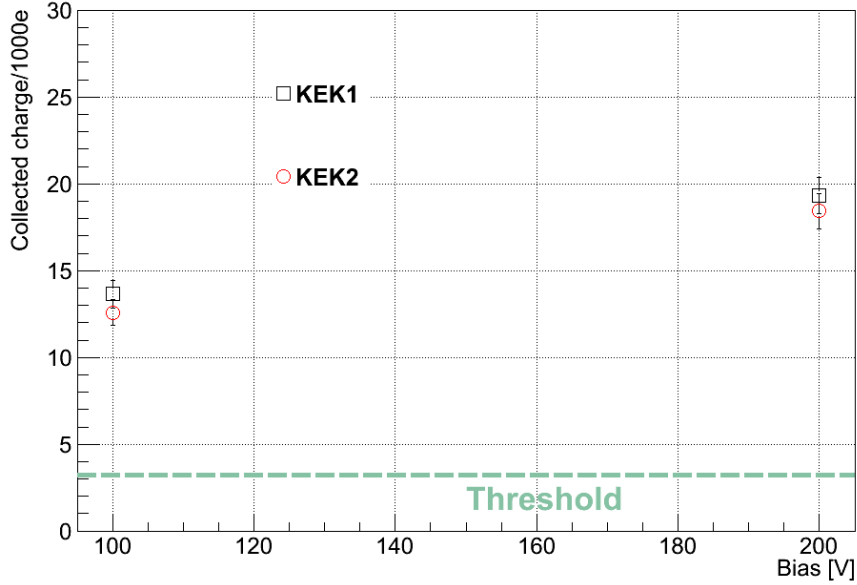


Figure 15. Collected charge as a function of the bias voltage for HPK samples; particles were impinging at different angles too. A threshold of 3200 e is indicated.

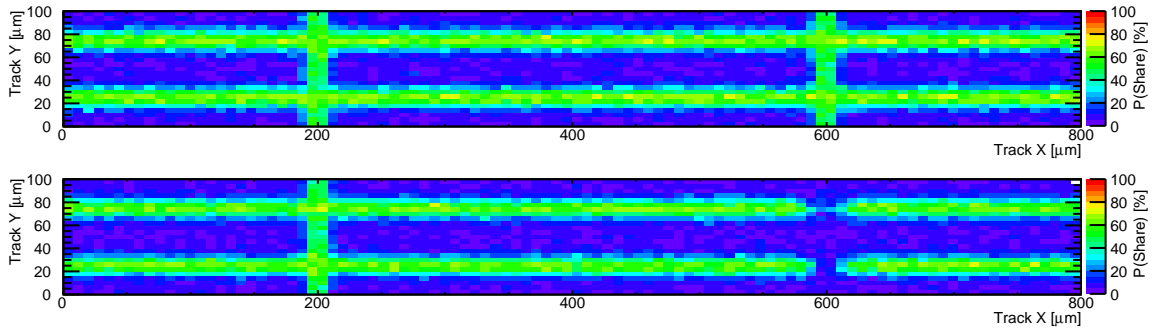


Figure 16. Charge sharing map for KEK1 (top) and KEK2 (bottom) at V_{bias} of 200 V.

329 both reactor neutrons (Jožef-Stefan Institute, Ljubljana) [18] and protons of 25 MeV (Karlsruhe
 330 Institute of Technology - KIT) [19] or 24 GeV (CERN) [12].

331 Most of the sensors follow the ATLAS Pixel detector sensor design with 16 guard rings and
 332 a thickness of $250 \mu\text{m}$. DO6 is a special sensor with only 11 guard rings overlapping the pixel
 333 region, designed to study possibilities to reduce the inactive area at the edge of the sensor (see
 334 section 6) and produced on $285 \mu\text{m}$ thick bulk material. The n-type sensors were produced at CiS,
 335 from Diffusion Oxygenized Float Zone (DOFZ), $\langle 111 \rangle$ oriented wafers; the wafer resistivity was
 336 in the range between 2 and $5 \text{ k}\Omega$. The depletion voltage was in the range between 40 and 100 V
 337 for $250 \mu\text{m}$ thick sensors and between 50 and 140 V for $285 \mu\text{m}$ thick sensors. The inter-pixel

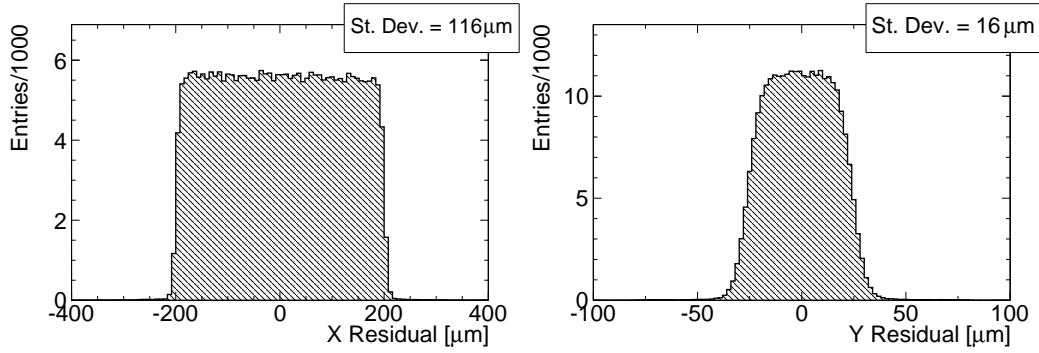


Figure 17. Cluster position residual distribution for non-irradiated sample KEK1 at V_{bias} of 200 V at normal incidence. Left: long pixel projection; right: short pixel projection.

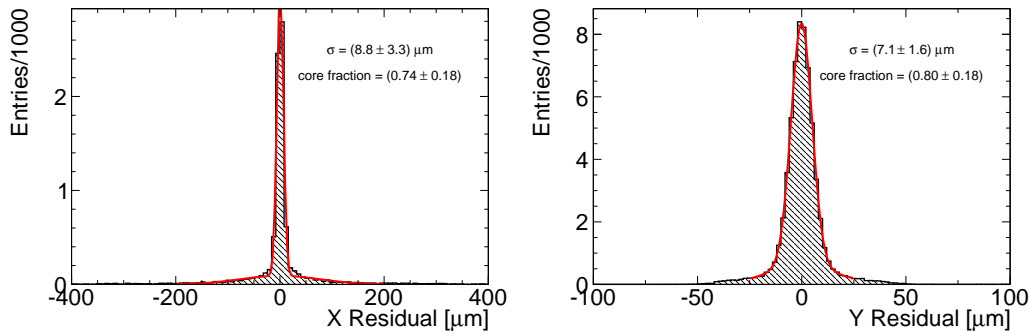


Figure 18. Residual distribution for non-irradiated KEK1 biased at 200 Volts clusters with 2 pixels. Left: long pixel projection; right: short pixel projection.

338 isolation is achieved by means of a “moderated” p-spray implantation [1].

339 A total of 5 irradiated n-in-n pixel sensors were tested. Table 5 summarizes the fluences to
 340 which the sensors were irradiated. See also [16].

name	thickness (μm)	fluence ($10^{15} \text{ n}_{\text{eq}}/\text{cm}^2$)	irradiation type
DO6	285	0	–
DO7	250	1	protons (KIT)
DO8	250	1	reactor neutrons
DO9	250	5	reactor neutrons
DO10	250	20	reactor neutrons

Table 5. Summary of irradiated n-in-n samples in the testbeams. KIT stands for 25 MeV energy proton irradiation.

341 5.1 Results

342 Measurements on n-in-n samples have been carried out at temperatures well below 0°C to reduce

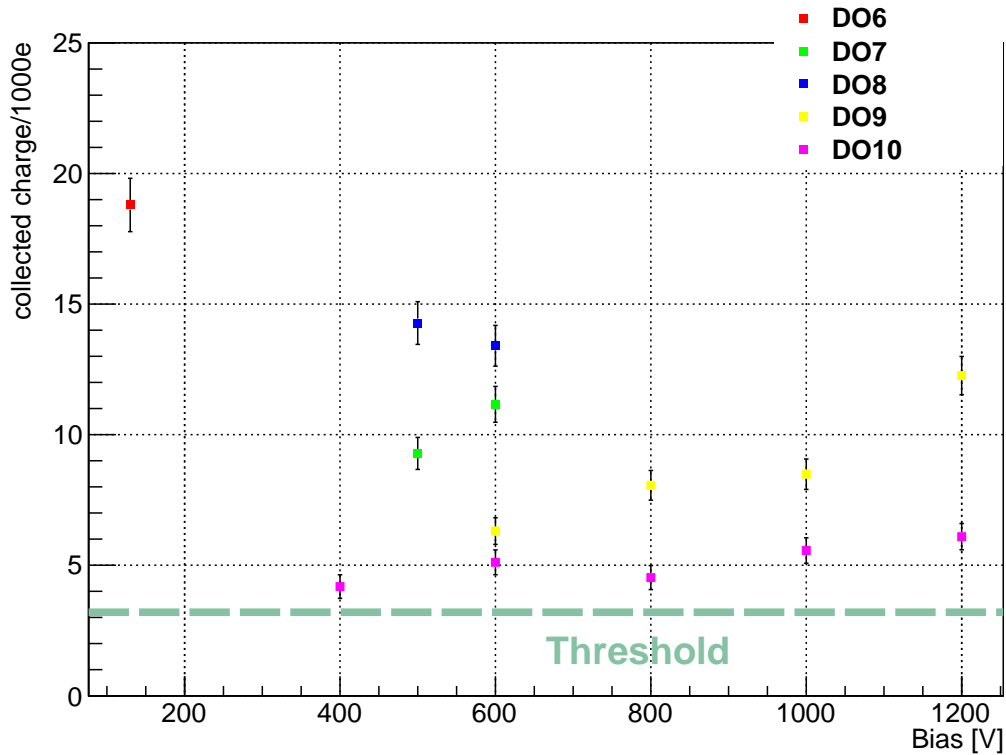


Figure 19. Collected charge as a function of bias voltage for n-in-n samples irradiated to different fluences (see details in the text). A threshold of 3200 e is indicated.

343 the large leakage current from irradiated sensors. As an example, we measured a leakage current
 344 of 24 μA (10 μA) for DO10 (DO9), at a bias voltage of 1200 V and at -47°C .

345 **Charge collection** One of the main effects of irradiation is the increased trapping, which leads
 346 to a reduced signal amplitude. As the trapping probability depends on the charge carrier velocity,
 347 the collected charge was measured as a function of the bias voltage. Figure 19 shows the results
 348 for all irradiated n-in-n samples in the two beam test periods; see also Table 5. A systematic
 349 error on the collected charge of 400 e is assumed, due to the finite charge resolution of the ToT
 350 mechanism; a 5% systematic uncertainty is also taken into account, due to non-uniformity in the
 351 injection capacitances.

352 After $5 \times 10^{15} \text{ n}_{\text{eq}}/\text{cm}^2$, the collected charge still exceeds 10 ke at a bias voltage of 1000 V. Even if
 353 the collected charge is shared equally between two neighboring pixels, this charge is sufficient to
 354 detect the hit with FE-I3.

355 Figure 20 top, shows that charge is predominantly lost in the region of the punch-through bias
 356 grid system.

357 At very high fluences ($2 \times 10^{16} \text{ n}_{\text{eq}}/\text{cm}^2$, DO10 sample) it is no longer possible to say which
 358 region is less efficient than the others, using the charge collection method (Figure 20, bottom).

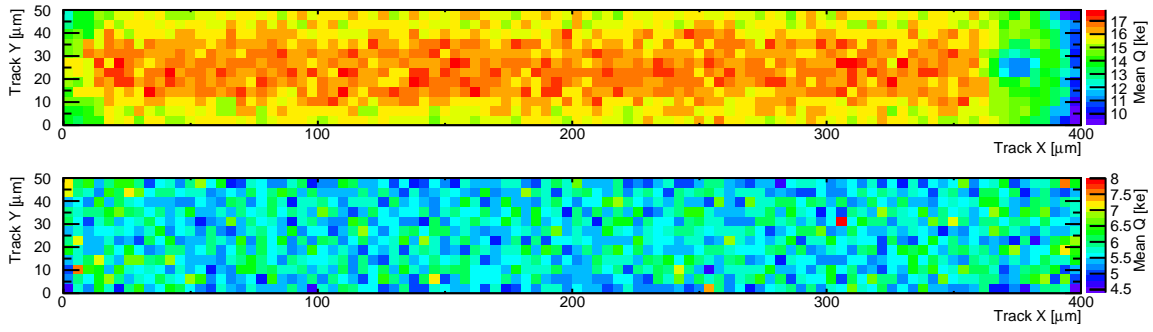


Figure 20. Charge collection within a pixel. Top: DO9 at $V_{bias}=1200$ V. Bottom: DO10 at $V_{bias}=1000$ V.

359 **Charge sharing** Figure 21 shows the charge sharing probability for DO9 at a bias voltage of
 360 1200 V. Reduced charge sharing probability is visible in the region of the bias dot and the bias grid
 361 network.⁶ Less charge is deposited here, so there is a higher probability for the second pixel in a
 362 two-pixel cluster to be below threshold. As only the bias trace makes the difference between both
 363 pixel sides, it might cause the lower charge sharing probability. Furthermore, one can see that the
 364 region of the bias dot is not affected.

365 While for DO9 a clear increase in charge sharing probability towards the edges of the pixel is
 366 visible, at higher fluence the collected charge becomes too small for any significant charge sharing
 367 to be observable. This can also be seen in the fractions of clusters with one, two, and more pixels.
 Figure 22 shows the fractions of one-pixel, two-pixel, and larger clusters as a function of the bias

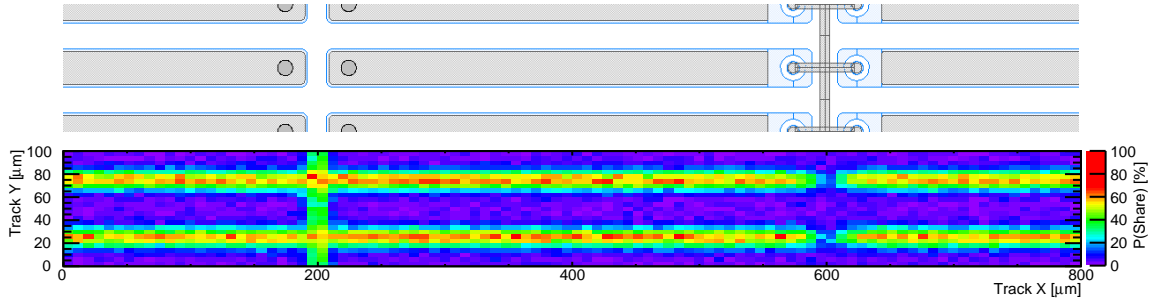


Figure 21. Top: Design of the sample of the region shown in the plot below. Bottom: Charge sharing probability for DO9 at $V_{bias}=1200$ V. Note the reduced charge sharing in the bias grid region on the right-hand side of the central pixel.

368
 369 voltage. It is evident, that with increasing bias voltage the cluster size increases, due to the reduced
 370 trapping. At a given voltage the fraction of 1-pixel clusters increases with fluence, as more charge
 371 is lost due to trapping.

372 For samples irradiated up to 5×10^{15} n_{eq}/cm^2 the cluster size increases slightly with bias voltage,
 373 while at 2×10^{16} n_{eq}/cm^2 the fraction of clusters with two or more hit pixels is very small and stays

⁶The bias grid network is an aluminum trace arranged on top of the intermediate pixel region connecting all bias dots.

nearly constant over the accessible voltage range.

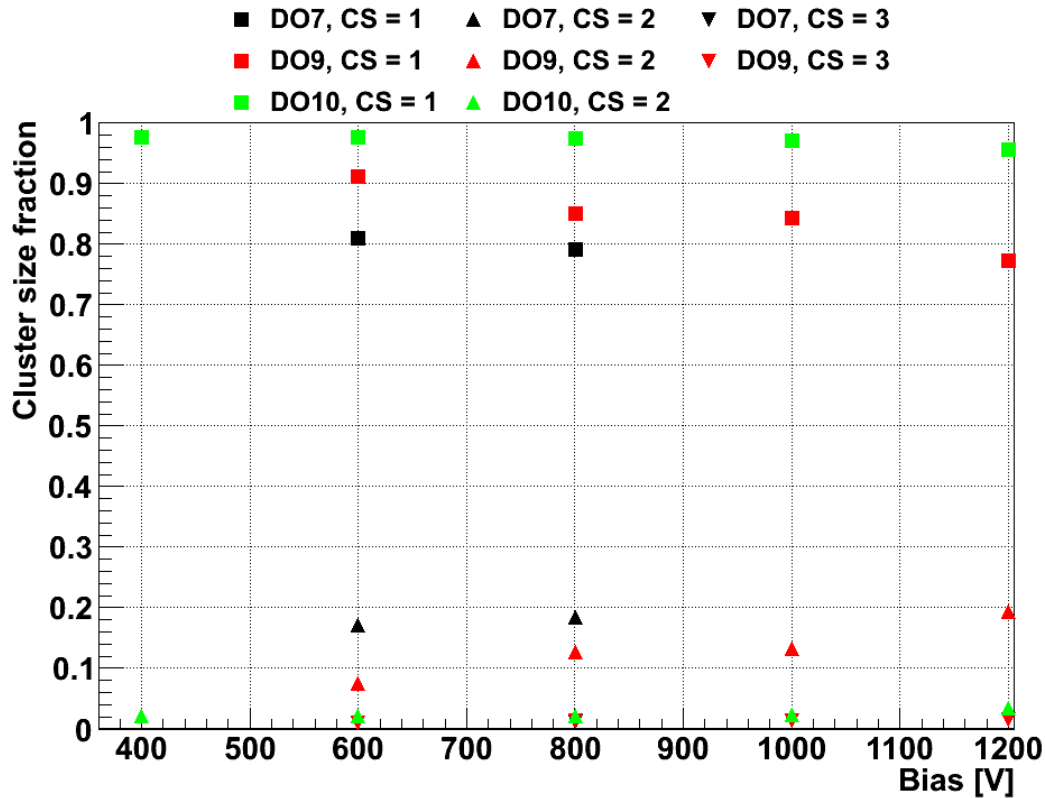


Figure 22. Fractions of 1-, 2-, and 3-hit clusters as function of bias voltage for irradiated n-in-n samples; see text for details. Error bars are too small to be visible.

374

375

376

377

378

379

380

Plotting the residual distribution for two-pixel clusters only allows the width of the charge sharing region between pixels to be determined. Figure 23 shows the distributions for DO9 ($5 \times 10^{15} \text{ n}_{\text{eq}}/\text{cm}^2$) and DO10 ($2 \times 10^{16} \text{ n}_{\text{eq}}/\text{cm}^2$). After correcting for the telescope resolution, the widths of the charge sharing regions are $7.1 \mu\text{m}$ and $7.7 \mu\text{m}$. These values correspond very well with the width found for an unirradiated sample of $6.4 \mu\text{m}$. This indicates that the lateral diffusion of the charge cloud does not change significantly with irradiation.

381

382

383

384

Residuals Figure 24 shows the residual distributions in the $50 \mu\text{m}$ pixel direction for the unirradiated sample (DO6) and the sample irradiated to $2 \times 10^{16} \text{ n}_{\text{eq}}/\text{cm}^2$, respectively. The widths of the distributions are $16 \mu\text{m}$ and $15.4 \mu\text{m}$, comparable with the expected digital resolution of $14.4 \mu\text{m}$. Thus, no influence of radiation damage on the spatial resolution can be observed.

385

6. Slim Edge

386

387

388

For slim edge studies the outermost pixels of a sample are of special interest. Therefore, the samples were mounted such that the edge of the sensor was well within the trigger acceptance window. Special analysis classes were written to investigate the characteristics of the edge pixels. The basic

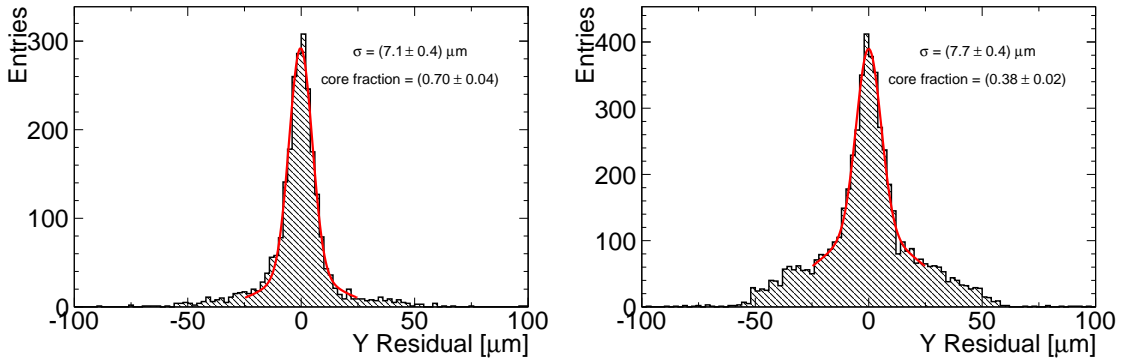


Figure 23. Residual distributions for 2-pixel clusters only. Shown are distributions samples irradiated to $5 \times 10^{15} \text{ n}_{\text{eq}}/\text{cm}^2$ (left: DO9, bias voltage 1000 V) and $2 \times 10^{16} \text{ n}_{\text{eq}}/\text{cm}^2$ (right, DO10, bias voltage 1200 V), respectively.

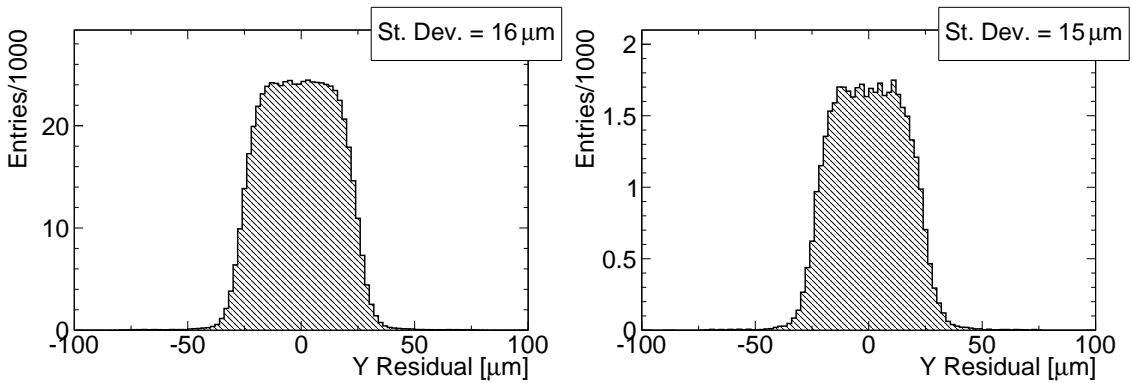


Figure 24. Residual distributions in the short pixel direction for an unirradiated sample (DO6, left) and a sample irradiated to $2 \times 10^{16} \text{ n}_{\text{eq}}/\text{cm}^2$ operated at a bias voltage of 1000 V (DO10, right). No deterioration of the spatial distribution with irradiation is visible.

389 principle is the same as for the charge collection analysis but instead of overlaying all pixels onto
 390 one single pixel, only pixels at the sensor edge are used and the special geometry is conserved in
 391 the overlay process.

392 For the IBL sensors the width of the inactive region at the edge of each sensor tile has to be re-
 393 duced significantly with respect to the approximately 1 mm wide region on each side of the current
 394 ATLAS Pixel detector sensors. One approach is to shift the guard-rings on the p^+ -side inwards.
 395 Two specially designed DUTs were tested to study the impact of an overlap between the active
 396 pixel region with the guard ring region, where the electric field in the sensor is inhomogeneous.
 397 In the DO6 sample, the overlap between active pixel region and guard ring region is $210 \mu\text{m}$, with
 398 the number of guard rings reduced to 11. In the DO3 sample groups of 10 pixels are shifted towards
 399 the edge of the sensor in steps of $25 \mu\text{m}$, increasing the area in which the pixels overlap with the
 400 guard-rings (see Figure 25).

401 The test structures were mounted such that the edge of the sensor was well in the center of the

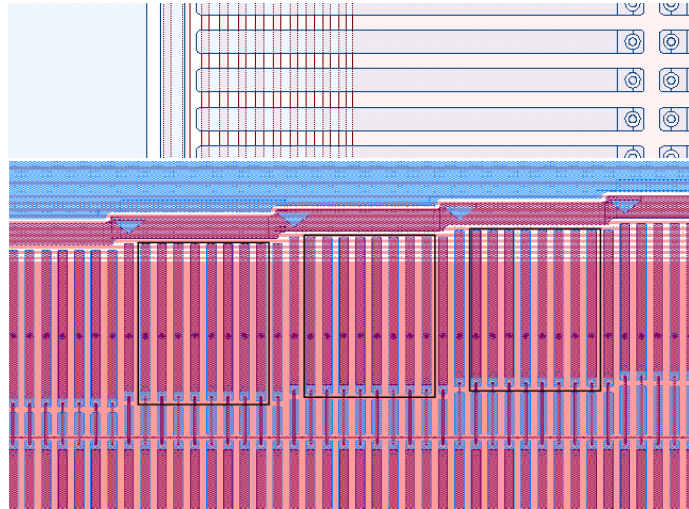


Figure 25. Test structures for slim edge studies. Top: DO6, the active pixel region overlaps the guard rings by $210\ \mu\text{m}$. Bottom: DO3, groups of 10 pixels shifted towards the edge of the sensor in steps of $25\ \mu\text{m}$.

402 trigger window, allowing to study charge collection in the shifted pixels in some detail. Figure 26
 403 shows the collected charge in the overlap region of DO6. With increasing distance from the bias
 404 voltage pad the collected charge decreases, due to the inhomogeneously formed depletion zone. It
 405 is evident that the collected charge is sufficient to ensure good hit efficiency up to about $200\ \mu\text{m}$
 406 from the edge of the bias voltage pad.

407

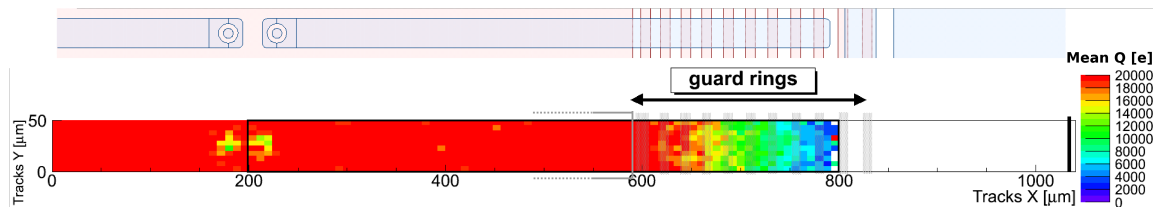


Figure 26. Charge collection in the pixels shifted underneath the guard rings.

408 Figure 27 shows the collected charge in the overlap region for the DO3 sample. Data from
 409 pixels with the same shift with respect to the edge of the bias voltage pad are plotted into one pixel.
 410 The drop in collected charge systematically occurs at the same distance from the bias voltage pad,
 411 regardless of the shift of the pixel. This indicates, that the loss of collected charge is indeed due to
 412 the depletion zone which is expected to be inhomogeneous along the x-axis (orthogonal to the bias
 413 voltage pad) but homogeneous along the y-axis (parallel to the bias voltage pad). Further studies
 414 of this kind can be found in [32].

415 7. Conclusion

416 Planar silicon sensors, have been tested in high energy pion beams at the CERN SPS North Area in

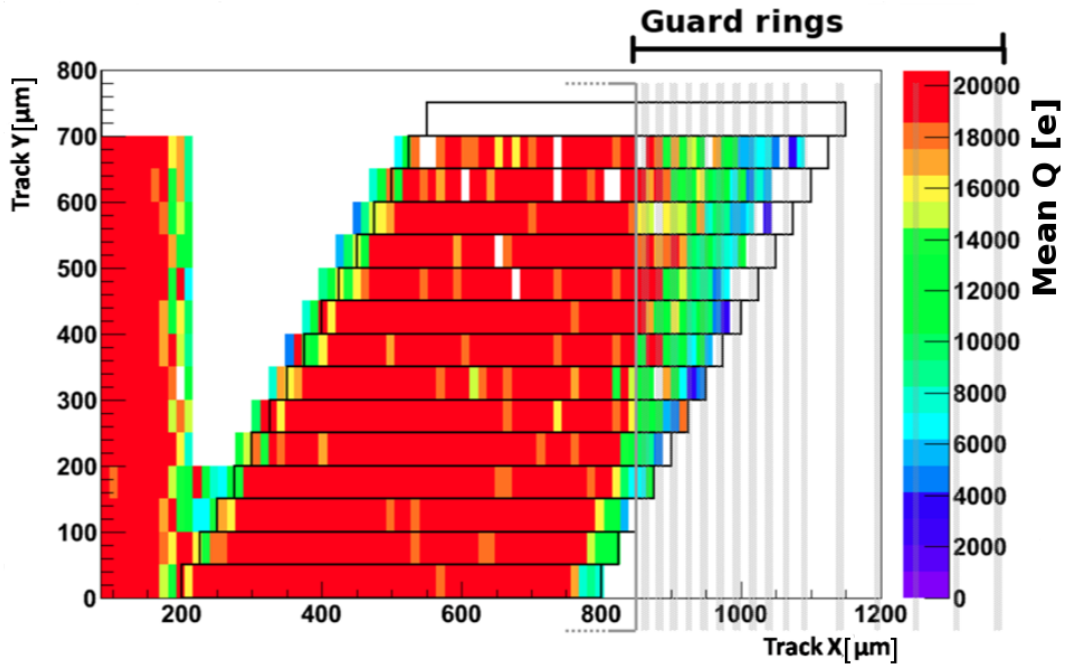


Figure 27. Charge collection in the pixels shifted underneath the guard rings.

417 2010 by the ATLAS Planar Pixel Sensors (PPS) collaboration. Different bulk materials, geometries,
 418 especially for the guard ring regions, biasing and isolation structures were examined.
 419 The goals of the measurement program were threefold: to demonstrate the suitability of p-bulk
 420 sensors for tracking purposes, to prove the radiation hardness of n-bulk sensors and to realize pixel
 421 sensors with reduced inactive edge area.

422 Pixelated p-bulk sensors produced by different vendors were tested to evaluate their perfor-
 423 mance, after irradiation too. In terms of the collected charge, charge sharing, and spatial resolution
 424 the performance of the p-bulk sensors was very good and comparable to that of n-bulk sensors.
 425 The issue of the high potential on the pixelated side of the sensor was tested and operation of the
 426 sensors was proven to be very stable.

427 The radiation hardness of n-bulk sensors was tested up to unprecedented fluences, with a
 428 maximum of $20 \times 10^{15} \text{ n}_{\text{eq}}/\text{cm}^2$. At a bias voltage of 1.2 kV a collected charge of about 6 ke was
 429 observed, corresponding to about one third of the collected charge before irradiation. Despite
 430 the rather small collected charge and the reduced charge sharing between pixels, no significant
 431 deterioration of the spatial resolution was observed.

432 In order to reduce the inactive area at the edge of n-bulk sensors, several modified sensor
 433 layouts were tested. The influence of a reduction of the number of guard rings and an increasing

434 overlap between the active pixel region and the guard ring region on the backside of the sensor
435 were studied. It was found that the charge collection efficiency reduces with increasing distance
436 from the edge of the bias voltage pad due to the inhomogeneously formed depletion zone in the
437 sensor. However, the collected charge is sufficient for reliable particle detection up to a distance
438 of about $200\ \mu\text{m}$ from the bias voltage pad. This was very encouraging for the planar ATLAS IBL
439 candidate design, which was finally designed employing the methods evaluated by the beam test
440 measurements described in this paper.

441 Acknowledgements

442 The authors would like to express their gratitude to V. Cindro, G. Kramberger and I. Mandić for
443 their valuable support with irradiations at the TRIGA reactor of the Jožef Stefan Institute, Ljubljana,
444 to A. Dierlamm for his help at the Irradiation Center, Karlsruhe, and to M. Glaser for his help
445 at the CERN PS irradiation facility.

446 The work has been partially performed in the framework of the CERN RD50 Collaboration.
447 This work is supported by the Commission of the European Communities under the 6th Framework
448 Programme “Structuring the European Research Area”, contract number RII3-026126.

449 We gratefully acknowledge the financial support of the German Federal Ministry of Science
450 and Education (BMBF) within their excellence program, in particular as part of the collaborative
451 research center “FSP 101-ATLAS, Physics on the TeV-scale at the Large Hadron Collider”.

452 We acknowledge the support of the Initiative and Networking Fund of the Helmholtz Association,
453 contract HA-101 (“Physics at the Terascale”).

454 References

- 455 [1] *ATLAS Pixel Detector Electronics and Sensors*,
456 The ATLAS collaboration, JINST 3 P07007, 2008
- 457 [2] *ATLAS Insertable B-Layer Technical Design Report*,
458 ATLAS TDR 19, CERN/LHCC 2010-013,
459 <http://cdsweb.cern.ch/record/1291633/files/ATLAS-TDR-019.pdf>
- 460 [3] *LHC near and medium term prospect*,
461 M. Lamont, <http://dx.doi.org/10.3204/DESY-PROC-2010-01/8>
- 462 [4] *Stragglings in thin silicon detectors*,
463 H. Bichsel, Rev. Mod. Phys. **60** 663 (1988)
- 464 [5] *Diamond pixel modules*,
465 D. Asner *et al.*, Nucl. Instr. Meth. **A636**, 125 - 129 (2011).
- 466 [6] *3D silicon pixel sensors: Recent test beam results*,
467 P. Hansson *et al.*, Nucl. Instr. Meth. **A628**, 216 - 220 (2011).
- 468 [7] ATLAS Upgrade Planar Pixel Sensor R&D Project,
469 see also <https://edms.cern.ch/document/966140>
- 470 [8] *Results from the EUDET telescope with high resolution planes*,
471 A. Bulgheroni *et al.*, Nucl. Instr. Meth. **A623**, 399-401 (2010).
- 472 [9] *The FEI3 readout chip for the ATLAS pixel detector*,
473 I. Perić *et al.*, Nucl. Instr. and Meth. **A565** 178 - 187 (2006).
- 474 [10] TurboDAQ
- 475 [11] *Test beam performance of the ATLAS Pixel Detector modules*,
476 A. Andreazza on behalf of the ATLAS Pixel Collaboration, Nucl. Instr. Meth. **A565**, 23 - 29 (2006).
- 477 [12] *New irradiation zones at the CERN-PS*,
478 M. Glaser *et al.*, Nucl. Instr. Meth. **A426**, 72 - 77 (1999).

- 479 [13] *Spatial resolution of silicon microstrip detectors*,
480 R. Turchetta Nucl. Instr. Meth. **A335**, 44 - 58 (1993).
- 481 [14] *Highly segmented thin microstrip detector with data-driven fast readout*,
482 M. Bomben *et al.*, Nucl. Instr. Meth. **A623** 159-161 (2010).
- 483 [15] *Design studies on sensors for the ATLAS Pixel Detector*,
484 F. Hüggling, Nucl. Instr. Meth. **A477** 143-149 (2002).
- 485 [16] *Radiation hardness studies of n^+ -in- n planar pixel sensors for the ATLAS upgrades*,
486 S. Altenheiner *et al.*, Nucl. Instr. Meth. **A658**, 25 - 29 (2011).
- 487 [17] *Development and operation of a testbeam setup for qualification studies of ATLAS pixel sensors*,
488 G. Troska, Ph. D. Thesis, TU Dortmund, 2012
- 489 [18] *Analysis of neutron flux distribution for the validation of computational methods for the optimization
490 of research reactor utilization*,
491 L. Snoj *et al.*, Appl. Rad. and Iso. **69** (2011) 136
- 492 [19] Irradiation Center of Karlsruhe Institute of Technology (KIT)
- 493 [20] *Characterization and performance of silicon n -in- p pixel detectors for the ATLAS upgrades*,
494 P. Weigell *et al.*, Nucl. Instr. and Meth. **A658** 36 - 40 (2011).
- 495 [21] *Measurements of spatial resolution of ATLAS pixel detectors*,
496 T. Lari *et al.*, Nucl. Instr. and Meth. **A465** 112 - 114 (2001).
- 497 [22] *Development of n -in- p silicon planar pixel sensors and flip-chip modules for very high radiation
498 environments*,
499 Y. Unno *et al.*, Nucl. Instr. and Meth. A **650** (2011), p. 129
- 500 [23] *Test Beam Measurements with the EUDET Pixel Telescope*,
501 J. Behr, <http://www.eudet.org>, EUDET-Report-2010-01
- 502 [24] *A Trigger/Timing Logic Unit for ILC Test-beams*,
503 D. Cussans, Contribution to “TWEPP-07 Topical Workshop on Electronics for Particle Physics”,
504 3-7 September 2007, Prague (Czech Republic)
- 505 [25] *A ten thousand frames per second readout MAPS for the EUDET beam telescope*,
506 C. Hu-Guo, CERN-2009-008
- 507 [26] *Jets at High Q^2 at HERA and Test Beam Measurements with EUDET Pixel Telescope*,
508 J. Behr, Dissertation & Ph. D. thesis (2010) - ZEUS, Universität Hamburg, Chapter 16
- 509 [27] *MILLIPEDE*,
510 V. Blobel, <http://www.desy.de/~blobel>
- 511 [28] *Full simulation of a testbeam experiment including modeling of the Bonn Atlas Telescope and Atlas
512 3D pixel silicon sensors*,
513 K. N. Sjøbæk, Thesis presented for the Master of Science degree in Experimental Particle Physics,
514 Department of Physics, University of Oslo, Appendix C
- 515 [29] *The Deterministic Annealing Filter*,
516 S. Fleischmann, CERN-THESIS-2007-011, pp.19 - 23
- 517 [30] *Notes on the fluence normalisation based on the NIEL scaling hypothesis*,
518 The ROSE Collaboration, Technical Note ROSE/TN/2000-02, CERN

519 [31] <http://root.cern.ch>

520 [32] *Planar slim-edge pixel sensors for the ATLAS upgrades,*
521 T. Wittig *et al*, 2012_JINST_7_C02051